Nanoscale

PAPER

View Article Online
View Journal | View Issue

Cite this: *Nanoscale*, 2024, **16**, 19239

Dual-mode detection for the total antioxidant capability of skincare products based on porous CuS@CdS@Au nanoshells†

Weimin Yang, Qi Ding, Xinhe Xing, Fang Wang, Hengwei Lin and Si Li *

Received 12th August 2024,
Accepted 23rd September 2024

DOI: 10.1039/d4nr03313b

rsc.li/nanoscale

The antioxidants in skincare products play a crucial role in delaying the aging process of the skin. With the growing variety of cosmetic products, it is essential to develop effective methods for measuring their total antioxidant capability (TAC). This study introduces a novel nanoenyzme, CuS@CdS@Au nanoshells (NSs), characterized by porous morphologies and composite materials, which demonstrate remarkable localized surface plasmon resonance (LSPR) effects, thereby enhancing their photocatalytic and photothermal properties. Under 808 nm laser irradiation, these nano-enzymes exhibited superior catalytic ability for TMB oxidation and temperature increases compared to CuS or CuS @Au NSs. The TMB absorption response and temperature increase showed high sensitivity to antioxidants such as ascorbic acid, glutathione, and ferulic acid, enabling the development of a dual-mode detection strategy for quantifying the TAC in skincare products without the need for complex pretreatments. Furthermore, the temperature response-based detection results proved to be more accurate than those derived from absorption response in recovery experiments. This research not only improves the reliability of antioxidant assessments but also provides a valuable tool for quality control in the skincare industry.

Introduction

As the outmost protective barrier, skin is vulnerable to oxidative stress caused by UV light, air pollution, and smoke. These oxidative stressors could exacerbate skin barrier dysfunction, damage, aging, and increase the risk of skin diseases.[1,2] To prevent oxidative disorder-induced skin aging and diseases, antioxidants that are vital in maintaining redox homeostasis and protecting the skin from oxidative stress have been added to skincare products, including ascorbic acid, ferulic acid, superoxide dismutase, astaxanthin, and so on.[3] However, there are still some shoddy products that may not undergo rigorous tests or don't work as advertised along with the rapid development of the skincare market. Detecting the antioxidant capability of skincare products not only can help consumers avoid being misled by false publicity and products with questionable quality but also can provide fulcrums and evidence for the research and development of enterprises. Therefore, it is important to develop reliable ways to measure the total antioxidant capability (TAC) in skincare products.

Traditional detection methods of TAC in skincare products or other sample matrices included liquid chromatography, and gas chromatography, *et al.*[4–7] These detection methods have high sensitivity and accuracy but still have limitations, such as high cost, complex sample preparation, and long test cycles, which make them unsuitable for conventional analysis. Exploring more convenient detection methods for TAC detection is highly necessary.

In recent years, nano-enzymes have attracted much attention since Yan's group found the peroxidase-liked catalytic ability of Fe_3O_4 nanoparticles (NPs),[8] which include many types, such as metals, metal oxides/sulfides, carbon-based materials, metal–organic frameworks, *etc.*[9–12] In the metal or copper sulfide nano-enzymes, localized surface plasmon resonance effect (LSPR) is a significant optical property that can largely enhance the photocatalytic activities of nano-enzymes when external light matches the vibration frequency of these nano-enzymes.[13,14] Moreover, the photothermal conversion ability is another important property of these nano-enzymes that have close relationships with the composition and morphology of nano-enzymes.[15–18] Developing nano-enzymes with particularly high LSPR effects can help to create more accurate detection methods for TAC based on photocatalysis and photothermal signals.

In this research, a novel nano-enzyme named CuS@CdS@Au was established with excellent LSPR effects by

International Joint Research Center for Photo-responsive Molecules and Materials, School of Chemical and Material Engineering, Jiangnan University, Wuxi, 214122, China. E-mail: sili@jiangnan.edu.cn

† Electronic supplementary information (ESI) available. See DOI: https://doi.org/10.1039/d4nr03313b

regulating the composition and morphology of nano-enzymes. When irradiated by a laser of 808 nm, the nano-enzymes can generate high-energy hot carriers. These hot carriers can cleave H_2O_2, catalyze the oxidation of TMB, and induce temperature elevations, but antioxidants can suppress these reactions and temperature changes. Based on these findings, a highly sensitive detection method is developed for the rapid and accurate detection of TAC in skincare products utilizing the dual-mode signals of absorption and temperature.

Results and discussion

Characterization of CuS@CdS@Au NSs

The construction process of CuS@CdS@Au NSs is displayed in Fig. 1a. Porous CuS nanoshells (NSs) were initially synthesized using the previously reported method (Fig. 1a and S1†).[19] Following this, CdS was grown on the surface of CuS in varying amounts (Fig. S2†). Subsequently, CuS@CdS@Au NSs were achieved by *in situ* reducing $HAuCl_4$ on the surface of CuS@CdS (Fig. S3†). The variation in CdS amounts was used to modulate the LSPR effect between CuS and Au, thereby enabling control over the photocatalytic and photothermal capabilities of CuS@CdS@Au NSs. To investigate the structure of CuS@CdS@Au NSs, NSs prepared with a concentration of 50 μM Cd^{2+} were initially characterized using transmission electron microscope (TEM) and dynamic light scattering (DLS).

From the TEM images, it could be observed that Au nanoparticles (NPs) were uniformly distributed on the surface of CuS@CdS (Fig. 1b and c). Furthermore, the size of CuS@CdS@Au NSs was larger than that of CuS and CuS@CdS (Fig. S4†). These results confirmed the successful construction of CuS@CdS@Au NSs. High-resolution TEM (HR-TEM), selective area electron diffraction (SAED), and energy dispersive spectroscopy (EDS) mapping were employed further to investigate the structure of CuS@CdS@Au NSs. According to the HR-TEM images, the crystal spacing of CuS (102), CdS (200), and Au (200) was measured to be 0.30, 0.27, and 0.20 nm (Fig. 1d and e), being consistent with the SAED results (Fig. 1f). The hollow center and porous shell of CuS@CdS@Au nano-enzyme could be observed in the high-angle annular dark-field scanning transmission electron microscope (HAADF-STEM) image (Fig. 1g). Furthermore, the EDS mapping of Cu, Cd, Au, and S elements proved the presence of CuS, CdS, and Au within CuS@CdS@Au NSs (Fig. 1h and i).

The X-ray diffraction (XRD) and X-ray photoelectron spectroscopy (XPS) measurements offered a more comprehensive understanding of the compositions and covalent states of CuS@CdS@Au NSs. The XRD spectra obtained from CuS@CdS@Au NSs matched well with the standard PDF card of CuS (PDF#00-006-0464), CdS (PDF#01-077-7280), and Au (PDF#01-071-4615), confirming the presence of CuS, CdS, and Au in CuS@CdS@Au NSs. In the elemental survey of CuS@CdS@Au NSs, high levels of C and O were detected in addition to Cu, Cd, S, and Au (Fig. S5a†), which likely originated from the polyvinyl pyrrolidone (PVP) that used as the stabilizer of CuS@CdS@Au NSs. The Cu 2p and Cu LMM scan indicated the valence state of Cu to be +2 (Fig. 2b and c);[20] while the Cd 3d and Cd MNN spectra suggested the valence state of Cd to be +2 (Fig. 2d and e). Furthermore, the high-resolution XPS spectra of Au and S revealed that the valence states of Au and S in CuS@CdS@Au NSs corresponded to 0 and −2, respectively (Fig. S5b and S5c†).[21,22] Additionally, CuS@CdS@Au NSs exhibited strong absorbance in the near-infrared range (Fig. S6†), which enabled photon irradiation using 808 nm laser.

Photocatalytic activity and photothermal conversion of CuS@CdS@Au NSs

Based on the structure investigation of CuS@CdS@Au NSs, their POD-like photocatalytic activity and photothermal conversion performance were investigated. When NSs were irradiated with 808 nm NIR light, numerous hot electrons (e^-) and hot holes (h^+) would be generated, which could break down the

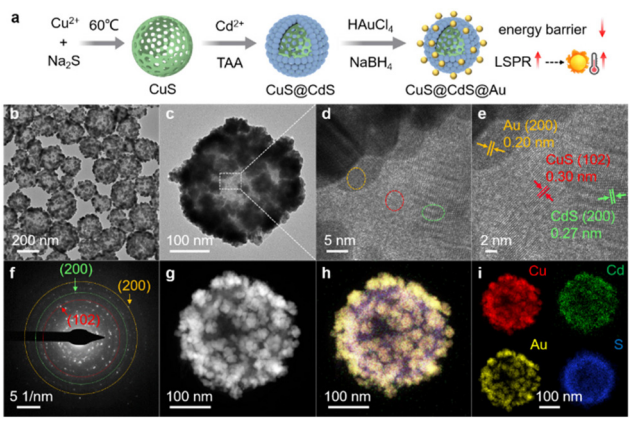

Fig. 1 (a) Schematic illustration of the synthetic process of CuS@CdS@Au NSs. (b and c) TEM images and (d and e) HR-TEM images of CuS@CdS@Au NSs. (f) SAED pattern of CuS@CdS@Au NSs. (g) HAADF-STEM image of CuS@CdS@Au NSs. (h and i) Elemental mapping images of Cu, Cd, Au, and S in CuS@CdS@Au NSs.

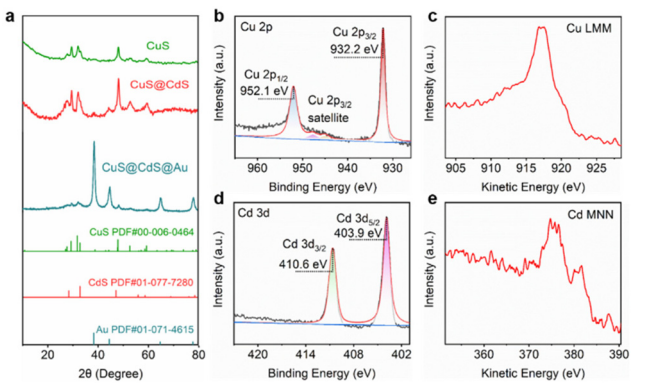

Fig. 2 (a) XRD patterns of CuS, CuS@CdS, and CuS@CdS@Au NSs and their corresponding standard PDF cards. XPS spectra of (b) Cu 2p, (c) Cu LMM, (d) Cd 3d, and (e) Cd MNN in CuS@CdS@Au NSs.

H_2O_2 that was adsorbed on the CuS@CdS@Au, leading to the production of ˙OH. Subsequently, the colorless TMB in the solution is oxidized into oxTMB by ˙OH, resulting in the color change to blue and absorbance increase at 652 nm (Fig. 3a, Fig. S7†).[23] Therefore, the absorption values at 652 nm were used to assess the photocatalytic abilities of CuS, CuS@CdS, and CuS@CdS@Au NSs (the concentration of Cu elements used for the catalysis evaluation was 60 ppm (Table S1†)). The results, as depicted in Fig. 3b and S8,† revealed that CuS, CuS@CdS, and CuS@CdS@Au NSs displayed POD-like catalytic activity even without photoirradiation. However, their catalytic abilities were significantly enhanced when irradiated with 808 nm laser for 5 min. Their catalytic kinetics were further measured and calculated according to the Michaelis–Menten equation (Fig. S9–S11†). Notably, CuS@CdS@Au NSs were demonstrated to have the fastest catalytic rate (V_{max}) and lowest Michaelis–Menten constant (K_m) value (Table S2†), indicating superior photocatalytic activity compared to CuS and CuS@CdS NSs. The presence of Au helps reduce the energy barrier, enhance the LSPR, and facilitate the separation of photogenerated electrons and holes. These factors contribute to the improved photocatalytic performance of CuS@CdS@Au NSs. These results highlight the importance of fine-tuning the components to enhance the catalytic capabilities of nano-enzymes.[24,25]

In addition to the photocatalytic ability, the photothermal conversion was also investigated. Under 808 nm laser irradiation for 5 min, the temperature of blank, CuS, CuS@CdS, and CuS@CdS@Au solutions increased to 32.2, 47.1, 49.8, and 65.4 °C, respectively (Fig. 3c, S12†). These results suggested that the presence of CdS minimally impacted the photothermal capability of CuS@CdS@Au. However, covering Au on the surface of CuS@CdS resulted in a 1.39-fold enhancement in photothermal conversion efficiency. Moreover, the temperature of the CuS@CdS@Au NSs increased significantly as the concentration and laser power increased (Fig. S13a and S13b†). Interestingly, after 5 irradiation cycles, little changes in temperature increases were observed (Fig. S13c†), highlighting the remarkable photothermal conversion stability of CuS@CdS@Au NSs. These results well illustrated that combining CuS, CdS, and Au into a unique morphology could enhance the photocatalytic and photothermal conversion capabilities of nano-enzymes. The enhanced photothermal conversion properties are primarily attributed to the presence of Au, which enhanced the LSPR effect of nano-enzyme.[26,27] This enhancement not only elevates the temperature through the photothermal effect but also enhances the catalytic performance of nano-enzymes.

To elucidate the origin of the enhanced catalytic performance, the catalytic efficiency of CuS@CdS@Au NSs at various temperatures was measured. The obtained absorbance intensity at 652 nm revealed a notable enhancement in catalytic activity with the temperature increase (Fig. S14†). However, the absorption at 652 nm obtained at 60 °C (Fig. S14†) remained lower than that obtained from CuS@CdS@Au NSs subjected to photon irradiation (Fig. 3b). This result revealed that the enhanced catalytic ability originated not only from the temperature elevation caused by the hot carriers generated during photoirradiation but also attributed to the reduced energy barrier and enhanced LSPR effect due to the presence of CdS and Au.[28,29]

Furthermore, apart from investigating the component effect on photocatalysis and photothermal conversion, CdS's quantity influence, which controlled the spacing between CuS and Au, was also studied, since it could potentially alter the LSPR effect of CuS@CdS@Au NSs. As depicted in Fig. 3d, CuS@CdS@Au NSs constructed with 50 μM Cd^{2+} displayed the highest photocatalytic efficiency, while the photothermal conversion ability had little increase. Consequently, CuS@CdS@Au NSs constructed with 50 μM Cd^{2+} were used as the nano-enzymes for subsequent antioxidant detection. To elucidate the photocatalytic mechanism of CuS@CdS@Au, the production of reactive oxygen species was detected (Fig. 3e). The measured results revealed that CuS@CdS@Au would cleave H_2O_2 and produce ˙OH under laser irradiation, which

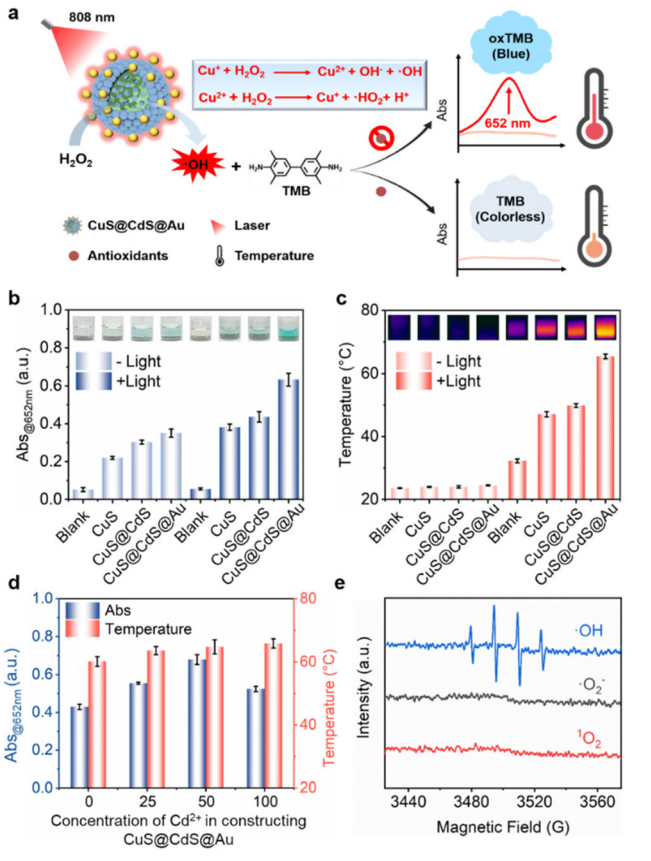

Fig. 3 (a) The colorimetric and temperature responses of CuS@CdS@Au NSs toward photoirridation in the absence or presence of antioxidants. (b) Absorption intensity (652 nm) and (c) temperature of the catalytic samples of blank, CuS, CuS@CdS, and CuS@CdS@Au with or without 808 nm laser irradiation. (d) The concentration effect of Cd^{2+} in constructing CuS@CdS@Au on the absorption at 652 nm and temperature of the catalytic system. (e) ESR spectra of CuS@CdS@Au NSs under 808 nm laser irradiation.

resulted in the oxidization of TMB and a corresponding absorption increase at 652 nm (Fig. S7†).

Dual-mode detection of TAC

CuS@CdS@Au NSs' detection capabilities toward TAC were measured based on their excellent photocatalytic and photothermal conversion capabilities. Because in the presence of antioxidants, ROS preferentially reacted with them, the TMB oxidation and temperature increase of the reaction systems could be significantly suppressed (Fig. 3a).

Ascorbic acid (AA), glutathione (GSH), and ferulic acid (FA) were selected as representative antioxidants to investigate the detection ability of CuS@CdS@Au NSs due to their inhibition toward the TMB oxidation (Fig. 4). Along with the concentration increase of AA, the blue color of detection solution gradually faded, and its absorption at 652 nm decreased progressively (Fig. 4a, b, and S15a†). When the concentration of AA ranged from 10 to 200 μM, the absorption intensity at 652 nm displayed a linear relationship with the logarithm of AA concentration (Fig. 4c). The limit of detection (LOD) of AA was calculated to be 0.11 μM. For GSH, similar color and absorption changes were observed (Fig. 4d, e, and S15b†), with a linear relationship between absorption intensity and the logarithm of GSH concentration in the range of 50 to 400 μM (Fig. 4f). The LOD of GSH was calculated to be 0.12 μM. However, in the presence of FA, the color of TMB changed from blue to yellow after the photocatalytic treatment, accompanied by a new absorption peak at 450 nm. The yellow color and absorption intensity at 450 nm became weaker as the concentration of FA increased (Fig. 4g, h, and S15c†). A linear relationship between the absorption intensity at 450 nm and the logarithm of FA concentration was established with the concentration changing from 5 to 100 μM (Fig. 4f). The LOD of FA was calculated to be 0.51 μM. Moreover, the color change of the detection solution from blue to yellow could indicate the presence of FA, and these changes can be attributed to the following reasons. TMB is characterized by two easily oxidizable amino groups, which can be oxidized, resulting in colorimetric changes by the sequential loss of electrons. Specifically, upon the loss of one electron, TMB transitions to a blue color, accompanied by an absorption peak at 652 nm. Conversely, the loss of two electrons causes TMB to exhibit a yellow color, with an absorption peak observed at 450 nm. In the presence of AA or GSH, TMB undergoes one-electron oxidation, resulting in a blue coloration and an absorption peak at 652 nm; thus, this wavelength was utilized to establish a linear relationship. In contrast, when TMB interacts with FA, it experiences two-electron oxidation, resulting in a yellow coloration and a corresponding absorption peak at 450 nm, which was used to establish the relevant linear relationship.[23]

Besides the color change of TMB, the presence of antioxidants could also inhibit the temperature increase of the detection solution. The concentration effects of AA, GSH, and FA on the temperature were investigated to establish the temperature responded detection method (Fig. 5). As the concentration of these antioxidants increased, the temperature decreased obviously (Fig. 5a, b, d, e, g, h, and S16†). When the concentration of AA, GSH, and FA ranged from 10 to 200 μM, 50 to 400 μM, and 5 to 100 μM, respectively, the linear relationships between the logarithm con-

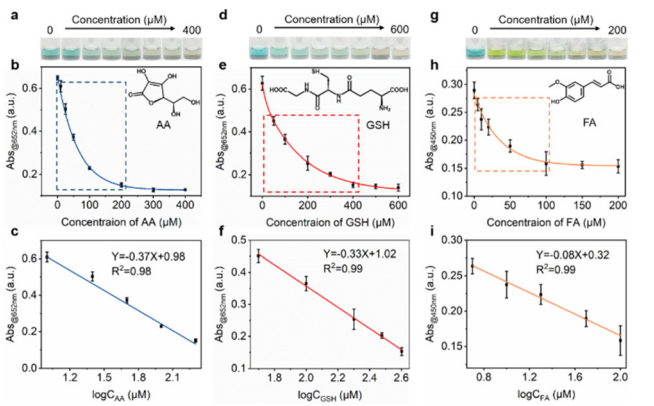

Fig. 4 Colorimetric detection of AA, GSH, and FA based on CuS@CdS@Au NSs. (a) Photograph and (b) absorption at 652 nm of the detected samples with different concentrations of AA. (c) The linear relationships between the absorption intensity at 652 nm and the logarithm of AA concentrations. (d) Photograph and (e) absorption at 652 nm of the detected samples with different concentrations of GSH. (f) The linear relationships between the absorption intensity at 652 nm and the logarithm of GSH concentrations. (g) Photograph and (h) absorption at 450 nm of the detected samples with different concentrations of FA. (i) The linear relationships between the absorption intensity at 450 nm and the logarithm of FA concentrations.

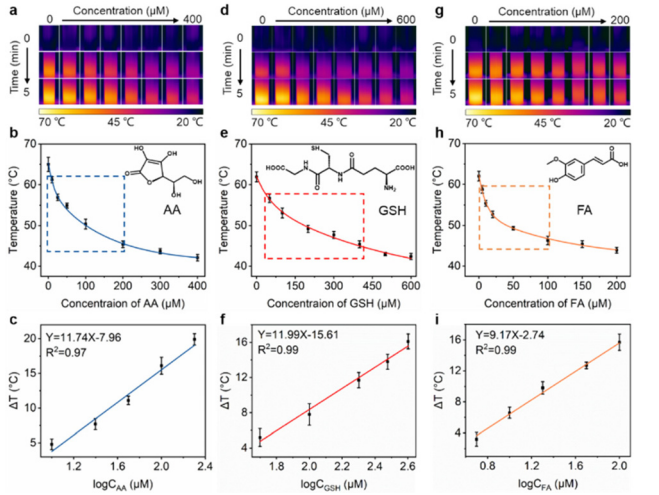

Fig. 5 Temperature detection of AA, GSH, and FA based on CuS@CdS@Au NSs. (a) Photothermal image and (b) temperature values of the detected samples with different concentrations of AA. (c) The linear relationships between temperature values and the logarithm of AA concentrations. (d) Photothermal image and (e) temperature values of the detected samples with different concentrations of GSH. (f) The linear relationships between temperature values and the logarithm of GSH concentrations. (g) Photothermal image and (h) temperature values of the detected samples with different concentrations of FA. (i) The linear relationships between temperature values and the logarithm of FA concentrations.

centrations of AA, GSH, and FA and the temperature were established (Fig. 5c, f, and i), respectively. The LODs of AA, GSH, and FA were calculated to be 0.32, 0.32, and 0.42 μM, respectively.

Moreover, the detection ability of CuS@CdS@Au NSs toward other kinds of metal ions and amino acids was also measured. The absorption at 652 nm and the temperature of the detection solution showed good responses to the molecules with antioxidant abilities, including cysteine (Cys), histidine (His), AA, GSH, and FA. The absorption intensities at 652 nm and the temperature of detection solutions were directly related to the antioxidant capabilities of these molecules (Fig. S17†). These results demonstrated that the antioxidants could be successfully detected based on the absorption and temperature signals of CuS@CdS@Au NSs.

TAC measurement of real samples

To verify the practicability of the established method, the TAC of four samples sold in the market was detected based on the absorption and temperature signals after being diluted to proper concentrations. The labeled antioxidant component in sample 1 was AA. According to the detection method, the concentration of AA was measured to be 477.16 ± 16.06 μM by the absorption intensity at 652 nm and 628.99 ± 74.12 μM by the temperature value (Fig. 6a). Sample 2 was labeled with a 10% mass concentration of AA, which concentration was calculated to be 567.79 mM. According to the detection method established with absorption intensity and temperature, the concentration of AA was measured to be 640.42 ± 31.99 mM by the absorption intensity at 652 nm and 504.21 ± 39.79 mM by the temperature value (Fig. 6a). The measured results were close to the labeled content on the products. Sample 3 contained 3% resveratrol and 3% FA, whose antioxidant capability was equal to 937.05 ± 41.07 mM AA calculated based on the absorption intensity at 652 nm and 992.64 ± 22.42 mM AA based on the temperature value (Fig. 6a). The presence of FA could be identified by the yellow color of the detection solution. The detection results demonstrated the higher antioxidant capability of resveratrol and FA.

Furthermore, the skincare product without antioxidants was spiked with FA at a final concentration of 100 μM to confirm the detection ability of the established method based on FA (sample 4). The measured concentrations obtained with the absorption at 450 nm and temperature value were calculated to be 77.47 ± 7.73 μM and 103.63 ± 8.61 μM, with recoveries ranging from 77.47 ± 7.73%, 103.63 ± 8.61% (Fig. 6b). The relative standard deviations (RSD) were calculated to be 9.98% and 8.31% (n = 3). These results illustrated that temperature-based detection was more accurate than absorption-based detection.

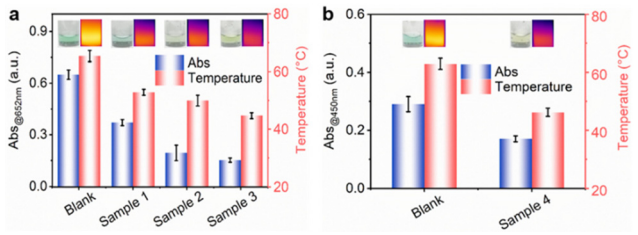

Fig. 6 Dual-mode TAC detection for skincare products based on the absorption and temperature of CuS@CdS@Au NSs. (a) Absorption intensity at 652 nm and temperature values obtained from different skincare products. (b) Absorption intensity at 450 nm and temperature changes of the sample containing FA.

Conclusions

In summary, CuS@CdS@Au NSs exhibiting an enhanced LSPR effect were synthesized through the regulation of their components and morphologies, leading to the generation of a significant quantity of hot carriers. These hot carriers facilitated superior photothermal conversion and photocatalytic performance in CuS@CdS@Au NSs. The photothermal conversion and TMB photo-oxidation were found to be simultaneously inhibited by antioxidants, which guided the establishment of a dual-mode detection method based on the absorption and temperature signals. This detection method allows for the quantitative evaluation of the TAC in commercially available skincare products, with temperature measurements yielding higher accuracy than TMB absorption changes. This study not only deepens our understanding of the photoconversion capabilities of nano-enzymes but also presents a new method for TAC detection in skincare products.

Author contributions

Weimin Yang: writing – original draft, investigation, formal analysis, data curation. Qi Ding: formal analysis. Xinhe Xing: investigation, methodology. Fang Wang: visualization. Hengwei Lin: investigation, supervision. Si Li: resources, writing – review & editing, supervision.

Data availability

The data supporting this article have been included as part of the ESI.†

Conflicts of interest

The authors declare that they have no known competing financial interests or personal relationships that could have appeared to influence the work reported in this paper.

Acknowledgements

This work was supported by the National Natural Science Foundation of China (32101142), the National Natural Science Foundation of Jiangsu Province (BK20221532), and the Fundamental Research Funds for the Central Universities (JUSRP622037).

References

1 Y. Gu, J. Han, C. Jiang and Y. Zhang, *Ageing Res. Rev.*, 2020, **59**, e101036.
2 A. Kammeyer and R. M. Luiten, *Ageing Res. Rev.*, 2015, **21**, 16–29.
3 J. Helberg and D. A. Pratt, *Chem. Soc. Rev.*, 2021, **50**, 7343–7358.
4 Z. Zhao, J. Zhao, N. Liang and L. Zhao, *Chemosphere*, 2020, **255**, e127004.
5 H. N. Zhao, X. Hu, M. Gonzalez, C. A. Rideout, G. C. Hobby, M. F. Fisher, C. J. McCormick, M. C. Dodd, K. E. Kim, Z. Tian and E. P. Kolodziej, *Environ. Sci. Technol.*, 2023, **57**, 2779–2791.
6 R. Jin, J. Shi, J. Yang, G. Yin, C. Xia, X. Wang, M. Liu and Y. Wu, *Environ. Chem. Lett.*, 2024, **22**, 997–1003.
7 F. Cacciola, P. Donato, D. Sciarrone, P. Dugo and L. Mondello, *Anal. Chem.*, 2017, **89**, 414–429.
8 L. Gao, J. Zhuang, L. Nie, J. Zhang, Y. Zhang, N. Gu, T. Wang, J. Feng, D. Yang, S. Perrett and X. Yan, *Nat. Nanotechnol.*, 2007, **2**, 577–583.
9 J. Chen, Q. Ma, M. Li, D. Chao, L. Huang, W. Wu, Y. Fang and S. Dong, *Nat. Commun.*, 2021, **12**, 3375.
10 W. Gao, J. He, L. Chen, X. Meng, Y. Ma, L. Cheng, K. Tu, X. Gao, C. Liu, M. Zhang, K. Fan, D. W. Pang and X. Yan, *Nat. Commun.*, 2023, **14**, 160.
11 S. Liu, Y. He, W. Zhang, T. Fu, L. Wang, Y. Zhang, Y. Xu, H. Sun and H. Zhao, *Small*, 2024, **20**, e2306522.
12 R. Zeng, K. Lian, B. Su, L. Lu, J. Lin, D. Tang, S. Lin and X. Wang, *Angew. Chem., Int. Ed.*, 2021, **60**, 25055–25062.
13 Y. Xin, K. Yu, L. Zhang, Y. Yang, H. Yuan, H. Li, L. Wang and J. Zeng, *Adv. Mater.*, 2021, **33**, e2008145.
14 W. Xu, H. Liu, D. Zhou, X. Chen, N. Ding, H. Song and H. Ågren, *Nano Today*, 2020, **33**, e100892.
15 S. Wu, P. Zhang, Z. Jiang, W. Zhang, X. Gong and Y. Wang, *ACS Appl. Mater. Interfaces*, 2022, **14**, 40191–40199.
16 Z. Li, J. Zi, X. Luan, Y. Zhong, M. Qu, Y. Wang and Z. Lian, *Adv. Funct. Mater.*, 2023, **33**, e2303069.
17 W. Liang, W. Qin, D. Li, Y. Wang, W. Guo, Y. Bi, Y. Sun and L. Jiang, *Appl. Catal., B*, 2022, **301**, e120808.
18 J. Zhao, S. Xue, R. Ji, B. Li and J. Li, *Chem. Soc. Rev.*, 2021, **50**, 12070–12097.
19 X. Deng, K. Li, X. Cai, B. Liu, Y. Wei, K. Deng, Z. Xie, Z. Wu, P. Ma, Z. Hou, Z. Cheng and J. Lin, *Adv. Mater.*, 2017, **29**, 1701266.
20 Q.-L. Hong, Y. Zhao, X. Ai, Y. Ding, F.-M. Li, P. Chen, P.-J. Jin and Y. Chen, *Chem. Eng. J.*, 2024, **482**, 148960.
21 Q. Xue, Z. Ge, Z. Yuan, J. Huang, B. He and Y. Chen, *Mater. Today Phys.*, 2023, **31**, 100980.
22 X. H. Wang, R. Yuan, S. B. Yin, Q. L. Hong, Q. G. Zhai, Y. C. Jiang, Y. Chen and S. N. Li, *Adv. Funct. Mater.*, 2023, **34**, 2310288.
23 X. Zhang, Q. Yang, Y. Lang, X. Jiang and P. Wu, *Anal. Chem.*, 2020, **92**, 12400–12406.
24 S. Li, F. Wang, X. Xing, X. Yue, S. Sun, H. Lin and C. Xu, *Adv. Healthcare Mater.*, 2024, **13**, e2303476.
25 B. Jiang, D. Duan, L. Gao, M. Zhou, K. Fan, Y. Tang, J. Xi, Y. Bi, Z. Tong, G. F. Gao, N. Xie, A. Tang, G. Nie, M. Liang and X. Yan, *Nat. Protoc.*, 2018, **13**, 1506–1520.
26 P. Bessel, A. Niebur, D. Kranz, J. Lauth and D. Dorfs, *Small*, 2023, **19**, e2206379.
27 N. Zhang, Y. Wang, M. Liu, T. Cheng, Z. Xing, Z. Li and W. Zhou, *Small*, 2024, **20**, e2400652.
28 S. Ma, K. Chen, Y.-H. Qiu, L.-L. Gong, G.-M. Pan, Y.-J. Lin, Z.-H. Hao, L. Zhou and Q.-Q. Wang, *J. Mater. Chem. A*, 2019, **7**, 3408–3414.
29 W.-Q. Zhao, Y. Liu, Z.-X. Zheng, L. Ma, K.-W. Xiong, X.-B. Chen and Q.-Q. Wang, *Chem. Eng. J.*, 2023, **475**, e146136.